ARTICLE   **Open Access**

Chip-based multimodal super-resolution microscopy for histological investigations of cryopreserved tissue sections

Luis E. Villegas-Hernández[1], Vishesh Dubey[1], Mona Nystad[2,3], Jean-Claude Tinguely[1], David A. Coucheron[1], Firehun T. Dullo[1], Anish Priyadarshi[1], Sebastian Acuña[1], Azeem Ahmad[1], José M. Mateos[4], Gery Barmettler[4], Urs Ziegler[4], Åsa Birna Birgisdottir[5,6], Aud-Malin Karlsson Hovd[7], Kristin Andreassen Fenton[7], Ganesh Acharya[2,8], Krishna Agarwal[1] and Balpreet Singh Ahluwalia [1,8]✉

Abstract

Histology involves the observation of structural features in tissues using a microscope. While diffraction-limited optical microscopes are commonly used in histological investigations, their resolving capabilities are insufficient to visualize details at subcellular level. Although a novel set of super-resolution optical microscopy techniques can fulfill the resolution demands in such cases, the system complexity, high operating cost, lack of multi-modality, and low-throughput imaging of these methods limit their wide adoption for histological analysis. In this study, we introduce the photonic chip as a feasible high-throughput microscopy platform for super-resolution imaging of histological samples. Using cryopreserved ultrathin tissue sections of human placenta, mouse kidney, pig heart, and zebrafish eye retina prepared by the Tokuyasu method, we demonstrate diverse imaging capabilities of the photonic chip including total internal reflection fluorescence microscopy, intensity fluctuation-based optical nanoscopy, single-molecule localization microscopy, and correlative light-electron microscopy. Our results validate the photonic chip as a feasible imaging platform for tissue sections and pave the way for the adoption of super-resolution high-throughput multimodal analysis of cryopreserved tissue samples both in research and clinical settings.

Introduction

Histology is the field of biology that studies the microanatomy and structure of tissues regarding their function in organisms. A typical histological analysis involves the extraction of a tissue sample from the body, fixation, and preservation followed by sectioning and labeling before observation through a microscope. In medical settings, histological investigations facilitate the identification and diagnosis of diseases, provide guidance for treatment, and assist in the prognosis of clinical outcomes.

Imaging throughput, contrast, and resolution are critical parameters for histological assessment. While whole slide imaging scanners provide fast imaging of several histological slides in a day, these automated optical microscopes are limited to a resolution power of ~250–500 nm (ref. [1]), which is insufficient for the observation of individual subcellular structures such as nanovesicles, filaments, tubules, brush border, gap junctions and several other intracellular features with an average size below ~250 nm. For decades, the visualization of such features was only possible through other imaging techniques such as electron microscopy[2–4], which supports a resolving power down to ~10 nm for fixed and embedded histological samples. While available published methods for fast[5] and automated correlation microscopy exist since years[6], the combination of traditionally lengthy sample preparation

Correspondence: Balpreet Singh Ahluwalia (balpreet.singh.ahluwalia@uit.no)
[1]Department of Physics and Technology, UiT The Arctic University of Norway, Klokkargårdsbakken N-9019, Tromsø, Norway
[2]Department of Clinical Medicine, Women's Health and Perinatology Research Group, UiT The Arctic University of Norway, Tromsø, Norway
Full list of author information is available at the end of the article
These authors contributed equally: Luis E. Villegas-Hernández, Vishesh Dubey

process, lack of specificity, low imaging throughput, system complexity, and high operational costs, has limited the adoption of electron microscopy in clinical settings, confining its implementation mostly to biology research.

Recently, the advent of super-resolution fluorescence optical microscopy techniques, also referred to as optical nanoscopy, bridged the resolution gap between the diffraction-limited optical microscopy and the electron microscopy methods, allowing for high-specificity imaging of biological specimens at high-resolution[7−9]. Present-day fluorescence-based super-resolution optical microscopy comprises a panel of methods that exploit engineered illumination and/or the photochemical and photokinetic properties of fluorescent markers to achieve high spatiotemporal resolution. These include structured illumination microscopy (SIM)[10], stimulated emission depletion microscopy (STED)[11], single-molecule localization microscopy (SMLM)[12,13], and intensity fluctuation-based optical nanoscopy techniques (IFON)[14].

While super-resolution fluorescence optical microscopy methods are commonly used in cell biology, their practical implementation in clinical settings for observations of tissue sections remains deferred due to multiple reasons: (a) the high labeling density of tissues poses challenges on super-resolution methods, especially for SMLM and IFON, where a high spatiotemporal sparsity is necessary for the reconstruction of structures beyond the diffraction limit of the microscope; (b) the susceptibility of the super-resolution methods to optical aberrations and light scattering introduced by refractive index variations across the samples[15]; (c) the imaging artifacts induced by autofluorescence signal of tissues[16]; and importantly, (d) the low-throughput, high-cost, lack of multi-modality, system complexity, and bulkiness of existing super-resolution optical microscopy setups.

Although limited work on using STED, SIM, and SMLM have been explored for super-resolution of histological samples[17−19], these methods fail to fulfill the throughput demands necessary for clinical assessment of tissue sections. For example, STED, albeit delivering a lateral resolution down to 20 nm (ref. [20]) and being a robust method to scattering challenges posed by tissues, is an inherently low-throughput point-scanning technique. Similarly, SMLM and SIM, despite being wide-field methods supporting sub-50 nm and ~110−130 nm lateral resolution respectively, are heavily dependent on the acquisition of multiple frames and subsequent reconstruction via post-processing algorithms. While SIM outperforms SMLM in terms of imaging speed, requiring only 9 or 15 images (2D/3D cases accordingly) as compared to the tens of thousands of images necessary for SMLM, the field of view obtained by commercial SIM systems is typically limited to about 40 μm × 40 μm. Importantly, among all the super-resolution methods,

SIM has been proposed for high-throughput imaging of tissue sections in clinical settings[18,21]. However, these approaches focused on the acquisition of large field of view images using low magnification and low numerical aperture objective lenses, compromising the lateral resolution to a maximum of 1.3 μm. In terms of system complexity, SMLM is simpler to implement as compared to SIM and STED, which require more sophisticated, bulkier, and costly setups. From an overall perspective, improvements in imaging throughput and reductions in system complexity, footprint, and cost are needed for the adoption of super-resolution fluorescence optical microscopy. Thus, to enable a widescale penetration in clinical settings, an imaging platform that can deliver different super-resolution capabilities using a standard optical microscopy setup is desirable.

Another important aspect necessary for the adoption of fluorescence-based super-resolution optical microscopy is the availability of a large selection of fluorophores. While SIM works with photo-stable and bright fluorophores, STED and SMLM are more restricted to a special type of fluorescent markers. Interestingly, some of the IFON techniques, such as the multiple signal classification algorithm (MUSICAL)[22], can exploit the pixel intensity variations arising not only from the intrinsic fluctuations of the fluorophores but also from the modulated emissions generated via engineered illumination, enabling a practical implementation with almost all kinds of fluorophores. Despite being an attractive route to follow for clinical applications, to the best of our knowledge the engineered illumination approach for IFON has not been explored in tissue imaging.

In recent years, photonic chip-based nanoscopy has emerged as a promising imaging platform for biological applications[23−26], supporting high-resolution, high-throughput, and multimodal capabilities. The technique consists of a photonic chip that is used both to hold the sample and to provide the excitation illumination necessary for fluorescent emission (Fig. 1a). The photonic chip is composed of two substrate layers of silicon (Si) and silicon dioxide (SiO_2), respectively, and a biocompatible waveguide core layer that transmits visible light, made of either silicon nitride (Si_3N_4)[24] or tantalum pentoxide (Ta_2O_5)[27]. Upon coupling, the excitation laser beam is tightly confined inside the optical waveguide layer and propagates through its geometry via total internal reflection (Fig. 1a, d). This generates an evanescent field on the top of the waveguide surface with an illumination reach of up to ~150−200 nm that is used to excite the fluorescent markers located in the vicinity of the waveguide surface (see Supplementary Information S1). The fluorescent emission is then collected by a standard upright microscope (Fig. 1c) equipped with conventional microscope objective lenses (Fig. 1d), enabling chip-based total
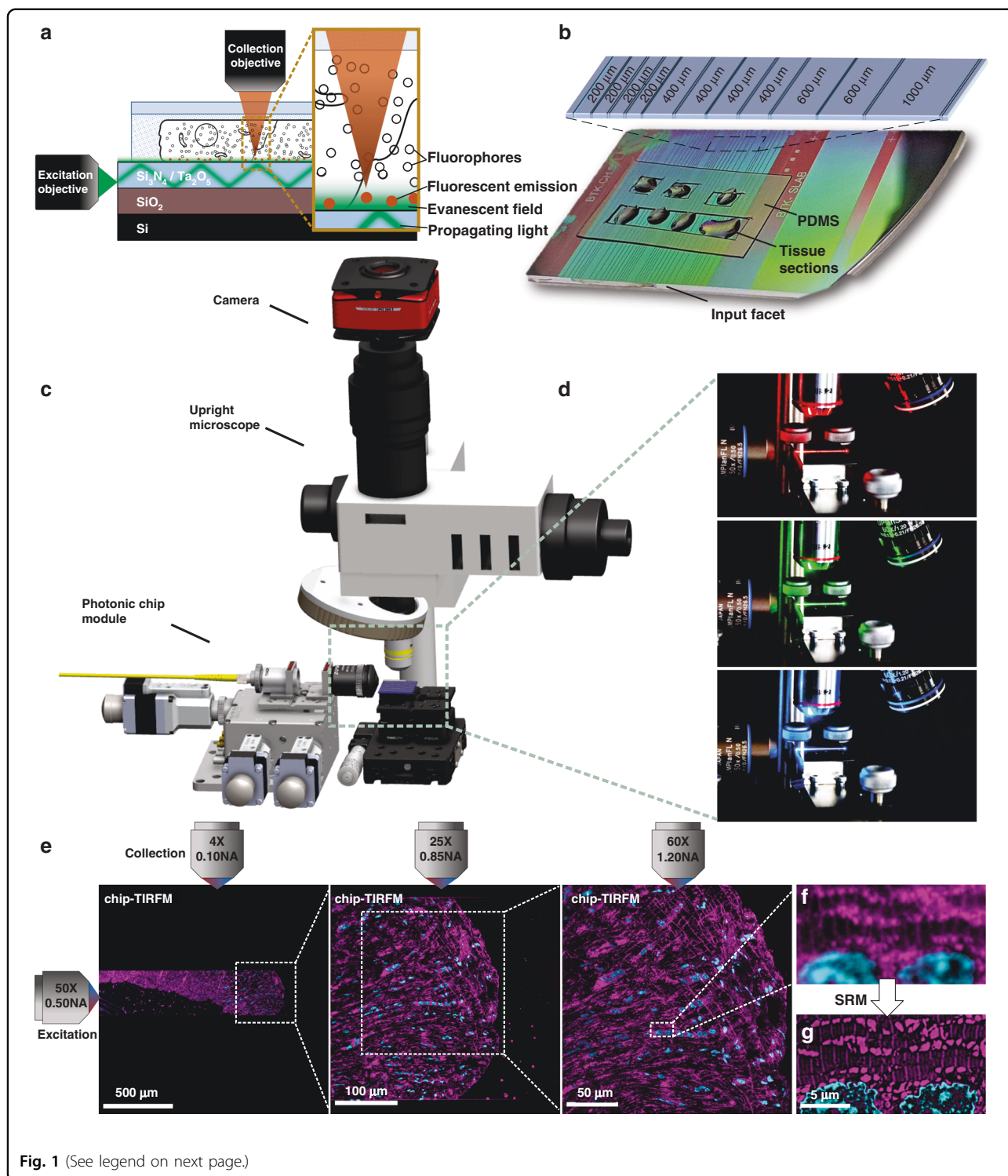
Fig. 1 (See legend on next page.)

internal reflection fluorescence microscopy over diverse fields of view (Fig. 1e).

To date, photonic chip-based microscopy studies have focused primarily on cellular biology[23–26,28,29], leaving on-chip histological imaging unexplored. In this work, we interrogate the photonic chip-based imaging platform to

address some of the challenges related to super-resolution imaging of tissue sections. We start by evaluating the viability of the photonic chip for diffraction-limited total internal reflection microscopy (chip-TIRFM). Then, we transition to more advanced chip-TIRFM based imaging methods such as SMLM, IFON, to conclude with a

(see figure on previous page)

Fig. 1 Schematic representation of the chip-based total internal reflection fluorescence microscopy (chip-TIRFM) setup. a Working principle of chip-TIRFM: upon coupling onto the input facet, the excitation light propagates through the waveguide core material due to total internal reflection. An evanescent field of ~150 nm height excites a thin layer of fluorescent dyes in the vicinity of the photonic chip surface, allowing for TIRFM imaging. **b** Top view of a photonic chip containing ultrathin Tokuyasu cryosections covered with a 1:1 cryoprotectant mixture of 2.3 M sucrose and 2% methylcellulose, and surrounded by a custom-made transparent polydimethylsiloxane (PDMS) frame. The inset illustrates the various strip waveguide widths available on the chip. **c** The chip-TIRFM setup is composed of a custom-made photonic chip module and a commercially available upright collection module. Upon coupling the excitation light on the photonic chip, the fluorescent signal is allowed through a filter set and captured with a scientific CMOS camera. **d** The photonic chip allows decoupling of the excitation and the collection light paths, enabling TIRFM imaging using conventional microscope objectives. Different wavelengths propagating on the waveguide core allow for multicolor TIRFM imaging. **e** TIRFM images of a 100 nm thick pig heart cryosection imaged on a photonic chip through different microscope objectives. Membranes in magenta and nuclei in cyan. Supplementary Information S9 provides a detailed view and an extended description of this tissue sample. **f** Magnified view of the diffraction-limited TIRFM image acquired with a 60X/1.20NA water immersion microscope objective. **g** Subsequent post-processing of the raw data enables super-resolution microscopy (SRM), allowing the visualization of structures beyond the diffraction limit of conventional optical microscopy. Image was taken by SIM

correlative light-electron microscopy (CLEM) analysis. Among the existing histological methods, we chose the Tokuyasu protocol[30] for the preparation of the tissue sections. This cryosectioning method provides excellent ultrastructural preservation, high molecular antigenicity, and a thin section thickness (70 nm to 1 μm) that assists both in reducing the light scattering artifacts associated with thicker samples[31] and in making optimal use of the illumination delivered by the photonic chip. We describe the staining protocols and the imaging parameters necessary for photonic chip-based microscopy of tissue samples and discuss the challenges and the advantages offered by this imaging platform for the investigation of tissue sections. By exploiting the engineered illumination delivered by the photonic chip-based microscopy, we validate this novel technique as a compact multimodal imaging platform suitable for the investigation of tissue sections, paving the way for future implementations of high-resolution, high-contrast, and high-throughput microscopy both in research and clinical settings. This is the first study of photonic chip-based super-resolution microscopy of tissue sections. Moreover, to the best of our knowledge, this is also the first super-resolution imaging study of human placenta and human kidney tissues using IFON methods.

Photonic chip-based microscopy for histology

Photonic chip-based illumination provides several advantages that can be exploited for super-resolution imaging of tissue sections, including:

a. The photonic chip allows decoupling of the excitation and the emission light paths, which translates into high-contrast images with improved imaging throughput. The propagating light enables a uniform illumination over the entire length of the waveguide while providing optical sectioning of the sample via evanescent field excitation[32]. As the illumination is provided by the photonic chip, the imaging objective lens can be freely changed (Fig. 1d), enabling the acquisition of images over large fields of view[26] (Fig. 1e), a feature not available in conventional TIRFM setups.

b. The multi-mode interference (MMI) illumination generated on the photonic chip assists in generating the necessary emission sparsity for diverse super-resolution fluorescent optical microscopy methods, as recently demonstrated via on-chip IFON[23,33], on-chip SMLM[23,26,34], and on-chip SIM[35]. Moreover, by using waveguide materials of high refractive index (for example, $n = 2$), it is possible both to tightly confine the light and to generate higher spatial frequencies as compared to free-space optical components[23,35], which can be exploited by IFON techniques such as MUSICAL. The MMI illumination further aids in providing spatiotemporal sparsity that is useful for highly dense and heterogeneous samples such as tissues.

c. Correlative imaging with other established methods including electron microscopy[36] and quantitative phase microscopy[27] can be seamlessly implemented on the photonic chip, expanding the opportunities both for routine analysis and for basic histology research.

d. The photonic chip-based microscopy can be implemented on standard optical microscopy platforms upon a few adaptations for the integration of a photonic chip module (Fig. 1c). The photonic chips can be manufactured in high-volumes following standard complementary metal-oxide-semiconductor (CMOS) photolithography processes, allowing for low operating costs in clinical settings.

Results
Chip-based multicolor TIRFM imaging

In this part of the study, we used chorionic villi tissue from the human placenta to assess the suitability of the photonic chip for histological observations. This tissue, present on the fetal side of the placenta, is responsible for

the air, nutrient, and waste exchange between the mother and the fetus during pregnancy[37], and is characterized by villous-like structures, namely villi, that sprout from the chorionic plate of the placenta to maximize the materno-fetal transfer processes and communication. When transversally sectioned, the chorionic villi appear in the form of rounded islands distributed across an open space surrounded by maternal blood, called the intervillous space.

Developed by Kiyoteru Tokuyasu in the '70s (refs. [38,39]), the so-called "Tokuyasu method" is still a gold standard protocol for ultrastructural analysis of cells and tissues[30]. Primarily established for EM techniques, recent studies have shown its versatility in fluorescence microscopy[40,41]. For chip-based multicolor TIRFM imaging, 400 nm thick chorionic villi cryosections were prepared following the Tokuyasu method (see detailed preparation protocol in Materials and Methods and Supplementary Information S2). After cutting the tissue blocks on a cryo-ultra-microtome, the sections were deposited onto a photonic chip previously coated with poly-L-lysine and equipped with a custom-made transparent polydimethylsiloxane (PDMS) frame (Fig. 1b). The membranes, F-actin, and nuclei were fluorescently stained following a direct-labeling approach using CellMask Deep Red, Phalloidin-Atto565, and Sytox Green, respectively (see Fig. 5 and Supplementary Information S7 and S8 for examples of indirect labeling, e.g., immunofluorescence, of diverse Tokuyasu cryosections).

For the excitation of the respective fluorescent dyes, three independent laser light wavelengths were used, namely 640, 561, and 488 nm (Fig. 1d). To obtain TIRF images (see detailed acquisition steps in Materials and Methods), the excitation light was coupled onto a single strip waveguide using a 50X/0.5NA microscope objective (Fig. 1c). Upon coupling, a multi-mode interference pattern was generated along the waveguide by the propagating light, which was then modulated by changing the position of the coupling objective relative to the chip (see Supplementary Information S3). To deliver a uniform illumination onto the sample, the coupling objective was laterally scanned along the input facet of the chip while individual frames were acquired. The fluorescent emission was collected by standard microscope objectives transitioning from lower to higher magnification to achieve different fields of view. Thereafter, the collected signal was averaged, pseudo-colored (membranes in red, F-actin in green, and nuclei in blue), and merged, allowing multicolor visualization of the different tissue components.

The large field of view provided by the 4X/0.1NA objective lens enabled us to locate the sample on the waveguide (Fig. 2a), while the 20X/0.45NA assisted for a contextual visualization of the tissue structure, supporting the identification of regions of interest for imaging with further magnification (white box in Fig. 2b). Finally, with the aid of a 60X/1.2NA water immersion objective lens (Fig. 2c), it was possible to visualize relevant structures of the chorionic villi, such as the apical layer of syncytio-trophoblastic cells, and the abundant fetal capillaries. Arguably, in this study, the absence of maternal red blood cells in the intervillous space can be attributed to the rinsing steps carried out along with the sample collection (see Materials and Methods). Figure 2c also allows the visualization of multinucleated cell aggregates that resemble the syncytial knots usually deported onto the maternal blood at different stages of the pregnancy[42]. Notably, the membrane marker not only allowed for an overall view of the tissue (Fig. 2b, c) but also enabled the distinction between adjacent cells such as a cytotrophoblast cell and a syncytiotrophoblast cell (white box in Fig. 2c and magnified view in Fig. 2d). Moreover, the observed F-actin signal (Fig. 2e) matched the locations reported in a previous study[43], allowing the identification of the microvilli brush border, the syncytiotrophoblastic's basal cell surface, and the capillary endothelial cells.

The cross-sectional dimensions of the Tokuyasu sections (typically ranging between 300 μm × 300 μm and 500 μm × 500 μm) perfectly suited the waveguide dimensions of the photonic chip used in this work. This configuration allows both complete imaging of the sample through a single optical waveguide and also supports independent illumination of adjacent waveguides on the chip with different tissue sections (Fig. 1b). This eliminates undesired excitation light of the samples outside the imaging region of interest, hence minimizing photobleaching. Moreover, the PDMS chambers (Fig. 1b) allowed multi-well experiments similarly to traditional microscope chamber slides, with the additional advantage of reducing the incubation volumes to ~10 to 20 μL per chamber, which translated into a cost-reduction of the fluorescence assays. After optimizing the sample preparation and imaging steps (see Optimization steps for successful on-chip tissue imaging), we were able to both fluorescently label and acquire chip-TIRFM images of placental tissue within a timeframe of three hours from cryosectioning to image post-processing. We also attempted chip-TIRFM imaging of formalin-fixed paraffin-embedded (FFPE) placental tissue sections (see Supplementary Information S10). While results were promising, we faced sample detachment issues that hampered the visualization of the overall FFPE slide. The optimization of these challenges will be carried out in a subsequent study.

For diffraction-limited imaging of tissue samples, such as shown in Fig. 2, the evanescent field illumination supported by TIRFM is not necessary. However, as it will be evident in further sections, for super-resolution methods such as SMLM and IFON the evanescent illumination generated by the photonic chip configuration
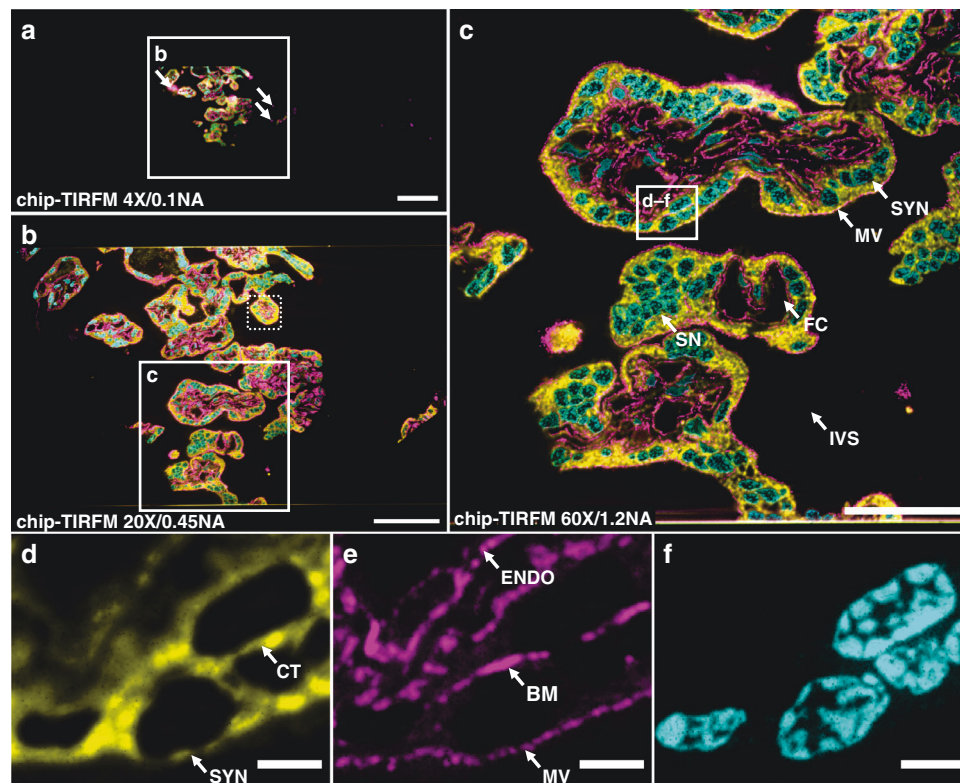
Fig. 2 Chip-based multicolor TIRFM imaging of a 400 nm placental tissue section prepared by Tokuyasu method. Membranes labeled with CellMask Deep Red (pseudo-colored in yellow), F-actin labeled with Phalloidin-Atto565 (pseudo-colored in magenta), and nuclei labeled with Sytox Green (pseudo-colored in cyan). **a** Large field of view chip-based multicolor TIRFM image acquired with a 4X/0.1NA microscope objective. The white arrows indicate the locations of unspecific binding of the F-actin marker to the waveguide. The white box represents the area imaged with a higher magnification objective lens in (**b**). **b** Chip-based multicolor TIRFM image acquired with a 20X/0.45NA microscope objective. The white box represents the area subsequently imaged with a higher magnification objective lens in (**c**). The white-dotted box illustrates the maximum field of view (50 μm × 50 μm) attainable in a conventional TIRFM setup. **c** Multicolor chip-TIRFM image acquired with a 60X/1.2NA microscope objective allows the identification of morphologically relevant structures of the chorionic villi such as the syncytiotrophoblastic cells (SYN), fetal capillaries (FC), syncytial knots (SN), and intervillous space (IVS) without maternal red blood cells due to thorough rinsing during sample preparation. The white box corresponds to the individual channels magnified in (**d**–**f**). **d** A magnified view of the membrane signal allows the distinction between a SYN and a cytotrophoblastic cell (CT). **e** A magnified view of the F-actin signal conforms to the expected location for this marker, in places such as the microvilli brush border (MV), the SYN's basal membrane (BM), and the capillary endothelial cell (ENDO). **f** Magnified view of syncytial and cytotrophoblast nuclei. Scale bars **a** 200 μm, **b** 100 μm, c 50 μm, **d**, **e** 5 μm

plays a key role in supporting optical sectioning of the specimen, reducing the out-of-focus light, increasing the signal-to-background ratio, and improving the axial resolution. Conventional TIRFM setups use oil-immersion high numerical aperture (N.A. 1.47−1.50) and high-magnification objective lenses (60X−100X) that limit their field of view to around 50 μm × 50 μm (ref. [26]) (dotted box in Fig. 2b). On contrary, the photonic chip-based TIRFM setup allows the use of essentially any imaging objective lens for the collection of the fluorescent signal, achieving scalable resolution and magnification on demand and opening possibilities for large TIRFM imaging areas up to the mm^2 scale (Fig. 2a, b). To this extent, the photonic chip-based TIRFM technique has the potential to outperform traditional ways of generating an evanescent field, which can be exploited for super-resolution imaging, as detailed in the next sections.

Chip-based SMLM imaging

In the previous section, we demonstrated the suitability of the photonic chip for diffraction-limited TIRFM imaging of tissues. Here, we explored on-chip super-resolution imaging of tissue samples using single-molecule localization microscopy (SMLM)[7]. SMLM comprises a set of methods that exploit the stochastic activation of individual fluorescent molecules to enable their precise localization within a sub-diffraction limited region. To achieve this, the fluorescent molecules are manipulated to obtain sparse blinking events over time. In practice, the majority of the fluorophores are switched off

(not emitting light), while only a small segment of them is switched on (emitting fluorescence). This implies the collection of several thousands of frames for the localization of the individual molecules in the sample.

There exist multiple variants of SMLM employing diverse switching mechanisms. Among them, the direct stochastic optical reconstruction microscopy (dSTORM) method supports conventional fluorophores, delivers a high photo-switching rate, and offers low photobleaching[44]. To explore the capabilities of the photonic chip for SMLM on histological samples, we used a 400 nm thick mouse kidney cryosection. We employed a dSTORM approach to visualize the nanostructural morphology of the filtration compartments present in the renal tissue, called glomeruli, whose physical dimensions are typically beyond the resolution limit of conventional optical microscopy and, therefore, often studied through electron microscopy.

The membranes and the nuclei were fluorescently stained with CellMask Deep Red and Sytox Green, respectively. All the preparation steps were performed identically to the chip-based multicolor TIRFM imaging experiments, except for the mounting medium that consisted of a water-based enzymatic oxygen scavenging system buffer[23,26] (see details in Supplementary Information S6). This oxygen scavenging buffer induces the blinking behavior by enhancing the probability of the fluorescent molecules to transition into the dark state, thereby contributing to the temporal sparsity of emission necessary for SMLM.

To find the features of interest, a TIRFM image of the sample was acquired (Fig. 3a) using low laser power to avoid photo-switching and reduce the chances of photobleaching. Next, the laser power was increased until sparse blinking was observed. The camera exposure time was set to around 30 ms to capture individual emission events of the membrane dye while the coupling objective was randomly scanned along the input facet of the chip. The collected image stack (>40,000 frames) was computationally processed to localize the spatial coordinates of the fluorophores, allowing for the reconstruction of a super-resolved image (Fig. 3b). A comparative view of both methods (Fig. 3c) reveals structural details in dSTORM that are not discernible in diffraction-limited TIRFM. In particular, dSTORM allows the visualization of a ~100 nm gap between the podocytes and the endothelial cells (see the empty gap between the white arrowheads in Fig. 3d, f), which is in agreement with the morphology of the glomerular basal membrane[45]. The identification of this feature, in particular, may be of critical value for a faster diagnosis of nephrotic diseases.

Chip-based SMLM/dSTORM supports three to fourfold resolution improvement over diffraction-limited imaging using a standard upright optical microscopy setup with a slight modification. Moreover, the chip-based SMLM/dSTORM approach benefits from the inherent advantage of decoupled illumination and collection light paths, which allows a user-defined choice of imaging objective lens without altering the TIRF excitation delivered by the chip. Recent advances in dye chemistry[46,47], in combination with further efforts in immunolabeling (see Supplementary Information S7 and S8) and system automation, could dramatically improve the imaging speed of chip-based SMLM, potentially assisting in the diagnostic of nephrotic diseases that, up to now, are identified via electron microscopy[48,49]. While chip-based illumination enables the imaging of large areas, the essential challenge of SMLM relies on the need for a large number of frames for the reconstruction of a super-resolved image. Therefore, for the practical implementation of chip-based microscopy in clinical settings, it is opportune to explore alternative imaging methods, e.g. IFON, with lower demands in the number of frames necessary for super-resolution.

Chip-based IFON imaging

To achieve a shorter acquisition time while maintaining imaging of large areas with improved contrast and resolution, we explored chip-based intensity fluctuation optical nanoscopy (IFON) of tissue samples. IFON comprises a set of techniques that exploit the photokinetic properties of fluorescent molecules to resolve structures beyond the diffraction limit of optical microscopes[14]. The techniques examine the stochastic emission of fluorophores through statistical analysis of the intensity levels of a given image stack, allowing the identification of fluorescent emitters with sub-pixel precision. Among the IFON techniques, the multiple signal classification algorithm (MUSICAL)[22] stands out as a promising tool for fast and reliable image reconstruction of biological data[14], achieving sub-diffraction resolution through low excitation intensities, fast acquisition, and relatively small datasets (100–1000 frames per image stack).

The main challenges to implementing IFON on histological samples are the high density and heterogeneity of the tissue samples. The spatiotemporal fluctuations are a decreasing function of the spatial density of the labels. In other words, a high density of labels results in a higher average signal at the cost of low variance in the fluorescence intensity over time. As a consequence, typically the IFON techniques are demonstrated on fine subcellular structures (e.g., actin filaments, microtubules, and mitochondria) fluorescently labeled on plated cells. Thus, densely labeled structures such as endoplasmic reticulum or lipid membranes are generally avoided. Tissue samples, with a higher density of labels, put even stronger demands on computational algorithms. Here, instead of relying only on the intrinsic fluctuations of the fluorophores, we
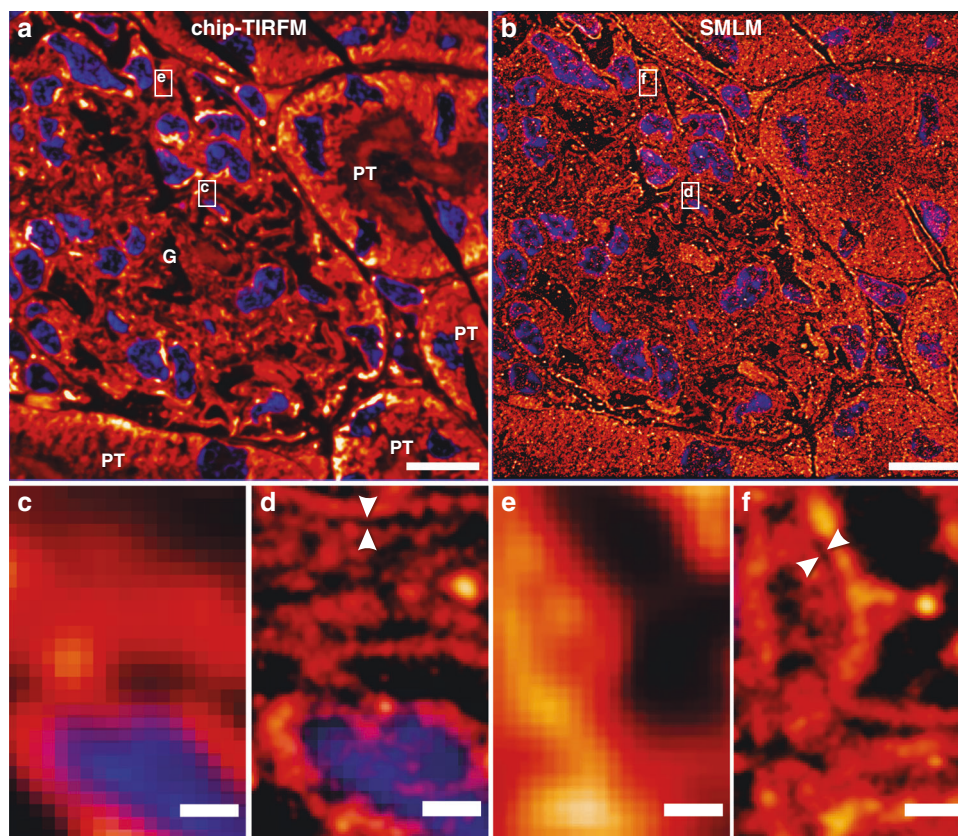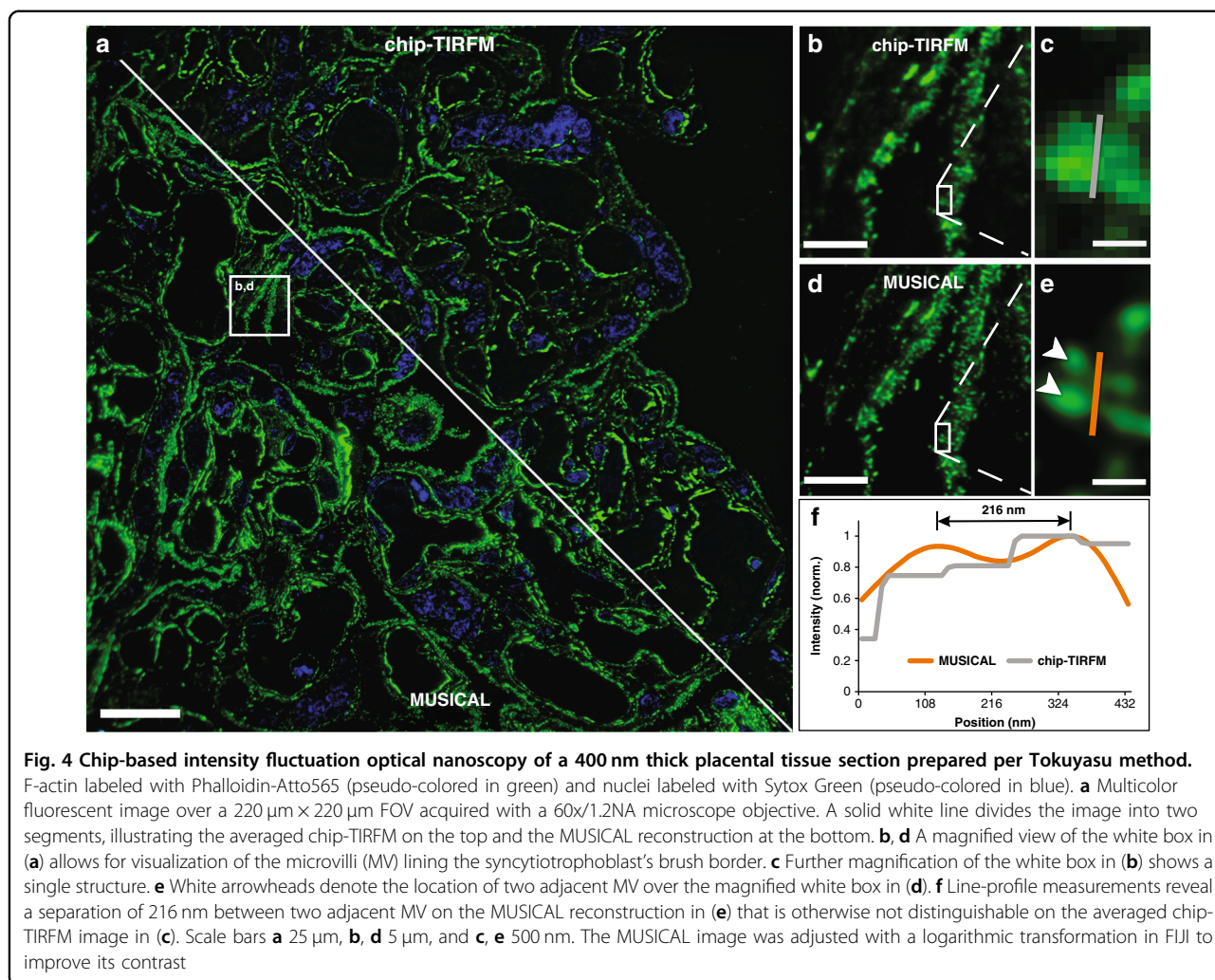
Fig. 3 Chip-based single-molecule localization microscopy of a 400 nm mouse kidney cryosection prepared by Tokuyasu method. Membranes labeled with CellMask Deep Red (pseudo-colored in orange) and nuclei labeled with Sytox Green (pseudo-colored in blue). Images were collected using a 60X/1.2NA water immersion microscope objective. **a** Chip-TIRFM image of a glomerulus (G) surrounded by proximal tubuli (PT). **b** Chip-based SMLM image reconstructed with the dSTORM algorithm. **c–f** A magnified view of the white rectangles in (**a**, **b**) allows the comparison between the chip-TIRFM and dSTORM images. In particular, the white arrowheads in the SMLM segments show a separation of ~100 nm between cellular structures that are otherwise not observable in the TIRFM segments. Arguably, this nanostructural feature is in agreement with the dimensions of the glomerular basal membrane present in this filtration compartment of the kidney. Scale bars **a**, **b** 10 µm, **c** 500 nm

propose to exploit also the intensity variations induced by the multi-mode interference (MMI) pattern (speckle-like illumination) generated by the photonic chip (see Supplementary Information S3). In this approach, on-chip MMI illumination patterns are modulated over time by scanning the illumination spot over the waveguide input facet. This modulates the fluorescence emissions from the fluorophores with the spatial intensity distribution of the illumination pattern at any given time. Due to the constructive and destructive interferences, bright and dark regions are formed, artificially introducing sparsity in the spatiotemporal fluctuations. In addition, due to the high refractive index of the waveguide core ($n = 2.1$ for Ta_2O_5 and $n = 2$ for Si_3N_4), the MMI pattern obtained on top of the waveguide surface is sub-diffraction limit and thus carries higher spatial frequencies than what can be obtained using free-space optics[23]. Here, we used such on-chip engineered illumination for super-resolution imaging using the MUSICAL method.

To interrogate the capability of the photonic chip for IFON-based imaging of histological samples, we used chorionic villi tissue cryosections from the human placenta. For IFON studies, we focused on the visualization of nanostructural features in the microvilli. The microvilli are actin-based membrane protrusions that increase the contact area between the syncytiotrophoblastic cells and the maternal blood, facilitating the biochemical exchange between the maternal and the fetal side, and supporting mechano-sensorial functions of the placenta[50]. Due to the physical dimensions of these structures (on average, 100 nm in diameter and 500 nm in length[2,3]), and their tight confinement along the apical side of the syncytiotrophoblastic cells, the morphological features of the microvilli are not discernible through conventional optical microscopy and, therefore, represent an ideal element to benchmark the resolution possibilities offered by chip-based IFON.

Fig. 4 Chip-based intensity fluctuation optical nanoscopy of a 400 nm thick placental tissue section prepared per Tokuyasu method. F-actin labeled with Phalloidin-Atto565 (pseudo-colored in green) and nuclei labeled with Sytox Green (pseudo-colored in blue). **a** Multicolor fluorescent image over a 220 μm × 220 μm FOV acquired with a 60x/1.2NA microscope objective. A solid white line divides the image into two segments, illustrating the averaged chip-TIRFM on the top and the MUSICAL reconstruction at the bottom. **b**, **d** A magnified view of the white box in (**a**) allows for visualization of the microvilli (MV) lining the syncytiotrophoblast's brush border. **c** Further magnification of the white box in (**b**) shows a single structure. **e** White arrowheads denote the location of two adjacent MV over the magnified white box in (**d**). **f** Line-profile measurements reveal a separation of 216 nm between two adjacent MV on the MUSICAL reconstruction in (**e**) that is otherwise not distinguishable on the averaged chip-TIRFM image in (**c**). Scale bars **a** 25 μm, **b**, **d** 5 μm, and **c**, **e** 500 nm. The MUSICAL image was adjusted with a logarithmic transformation in FIJI to improve its contrast

The samples were prepared and imaged with a 60X/1.2NA microscope objective following the steps described for Chip-based multicolor TIRFM imaging. To avoid unspecific background signal, only the F-actin and nuclei markers were used (Phalloidin-Atto565 and Sytox Green, respectively). Further, the 500-frames image stack corresponding to the F-actin was analyzed with MUSICAL, resulting in a super-resolved and improved contrast image over a field of view of 220 μm × 220 μm (Fig. 4a). The implementation of a soft thresholding scheme in MUSICAL[51] allowed the identification of individual microvilli along the syncytiotrophoblast's brush border (Fig. 4d), which were otherwise unclear in the averaged chip-TIRFM image (Fig. 4b). The resolution enhancement of MUSICAL was quantified in two different ways: (a) by performing line-profile measurements over two adjacent microvilli (Fig. 4c, e); and (b) by decorrelation analysis[52]. In the first case, the MUSICAL reconstruction (Fig. 4e) revealed a 216 nm separation between two microvilli, whereas the diffraction-limited chip-TIRFM image

(Fig. 4c) showed them as a single–merged–element. In the second case (see Supplementary Information S11), we were able to estimate a resolution of 195 nm on the MUSICAL reconstruction, compared to the 268 nm estimated for the chip-TIRFM counterpart. On-chip MUSICAL not only increases the resolution but improves the contrast of the image, which is a valuable parameter during visual investigations of tissue sections.

A recent study reported the visualization of individual microvilli with a twofold resolution improvement employing 3D-SIM[53]. Although several experts have proposed SIM as the fastest SRM technique for histological analysis[18,21,54,55], the typical FOV of this method with high-magnification microscope objectives (for example, 60X/1.42NA) is about 40 μm × 40 μm. Therefore, to match the same field of view achieved with the photonic chip, a tile mosaic of 7 × 7 SIM images would be required (see Supplementary Information S12). For conventional 3D-SIM, this not only implies a prolonged time for the data acquisition, but also a lengthy image

reconstruction that rounds up to 2.5 h. On contrary, the MUSICAL implementation we used here was able to obtain a high-resolution image over a large field of view within a combined collection and processing time of ~10 min for the 500-frames acquired on the photonic chip. While a 2D-SIM approach could potentially match, or even exceed, the acquisition and processing time of chip-based IFON, the photonic chip still outperforms 2D-SIM when it comes to the field of view size, system complexity, and cost.

From a practical perspective, the high-resolution visualization over large areas supported by chip-based IFON opens the door for improved assessment of placental microstructure both for basic research as well as for clinical assessment of placental dysfunctions associated with morphological changes in the microvilli, as documented in pre-eclampsia[2].

Chip-based CLEM imaging

Combining the specificity of fluorescence microscopy with the high resolution of electron microscopy allows the visualization of proteins of interest along with the ultrastructural context of the tissues. Although recent reports have proposed silicon wafers for correlative light and electron microscopy (CLEM)[56,57], they employed EPI-illumination through high-magnification microscope objectives, providing a limited field of view of the fluorescent signal. Here, we employed zebrafish eye retina cryosections of 110 nm thickness to demonstrate the compatibility of the chip platform with CLEM studies. Zebrafish is a well-established model for the study of retinal diseases[58]. The samples were prepared in the same manner as the placental and renal sections, except for the initial washing steps of the cryoprotectant. We found that the optimal washing temperature of the sucrose-methylcellulose solution for these samples was 0 °C, over an incubation time of 20 min (see detailed protocol in Materials and Methods). Three structures were labeled for the study: (a) the F-actin filaments, (b) the nuclei, and (c) the outer mitochondrial membrane. The first two structures were labeled through direct markers using Texas Red-X Phalloidin and Sytox Green, respectively, whereas the latter was labeled by immunofluorescence using rabbit anti-Tomm20 as a primary antibody, and Alexa Fluor 647-conjugated donkey anti-rabbit as a secondary antibody.

The samples were first imaged in chip-based TIRFM mode for each channel using a 60X/1.2NA to obtain a diffraction-limited multicolor image (Fig. 5a). Thereafter, the sections were platinum-coated and imaged on a scanning electron microscope over the same region of interest (Fig. 5b). A magnified view of the TIRFM image (Fig. 5c) allows for the observation of the F-actin filaments lining the outer segments of the photoreceptors

(in green), as well as the mitochondria clusters (in magenta), and the location of the nuclei (in cyan). The same TIRFM dataset is used for post-processing through MUSICAL, allowing for a precise correlation of both the F-actin and the mitochondrial signals with the corresponding SEM image (Fig. 5d–f).

Notably, the waveguide widths on the chip not only accommodated the whole zebrafish retina but also allowed the observation of several serial sections in a ribbon (see Supplementary information S14). Also, the combination of the thin section thickness of the Tokuyasu samples with the limited extent of the evanescent field dramatically improved the axial resolution of the fluorescent signal, enabling high-contrast images. Put together, these features are advantageous for confirming signal specificity throughout different subcellular compartments, opening up the possibility for 3D-stacking via serial section imaging[59,60]. Moreover, the flatness of the chip serves as an optimal platform for SEM, allowing autonomous imaging over large areas. A simple thin layer of platinum deposited on top of the chip minimizes the charging effects and enables a good correlation between the light and the electron microscopy images. Importantly, the photonic chip can incorporate coordinate landmarkings to facilitate the location and further correlation of the ROIs under study[36]. Lastly, the chip-based CLEM strategy presented here, in combination with the Tokuyasu method, can be executed within one working day from the sample sectioning steps to the SEM imaging, implying a significant time improvement as compared to the typical one-week imaging throughput associated with most CLEM approaches[41].

Optimization steps for successful on-chip tissue imaging

The experimental challenges of this study were mainly related to sample labeling and image acquisition. In the first place, the membrane tags investigated for labeling, namely CellMask Deep Red (CMDR), CellMask Orange (CMO), DiI, and DiO, showed high affinity to the photonic chip surface, inducing a high-background signal upon coupling of the excitation light onto the waveguides. Also, the combination of F-actin markers (Phalloidin-Atto647N, Phalloidin-Atto565) together with the CellMask family dyes (CMO and CMDR) led to the appearance of labeling artifacts in the form of dense spots (see white arrows in Fig. 2a), hampering the quality of the acquired images. We observed that after an initial bleaching step of the membrane dye (see Supplementary Information S4), the remaining fluorescent signal at the sample was generally stable through the image acquisition, allowing continuous imaging over prolonged timescales (>5 min). We hypothesize that due to the exponential decay of the evanescent field (see Supplementary Information S1), the fluorophores in close
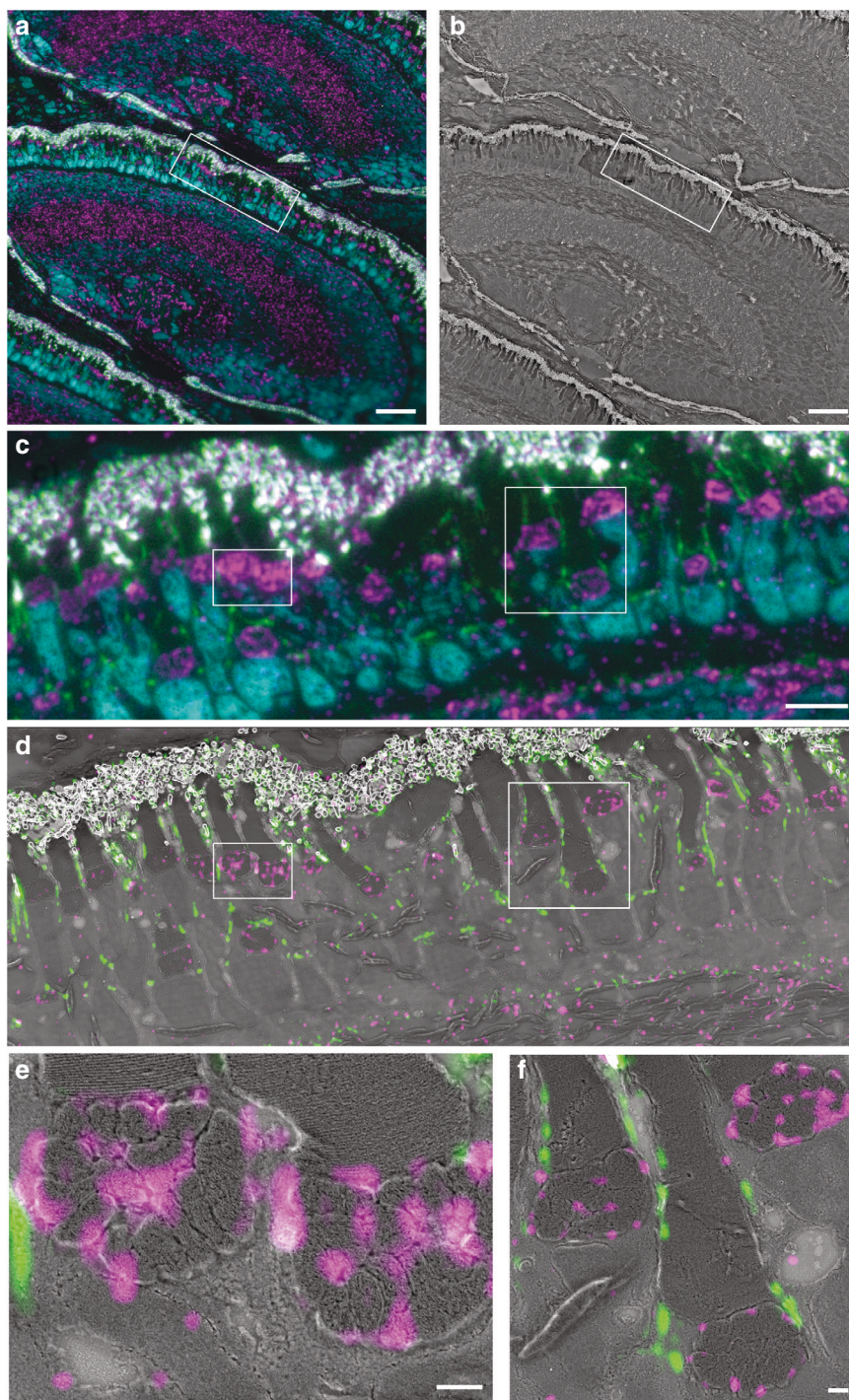
Fig. 5 Chip-based CLEM imaging of a 110 nm thick zebrafish retina cryosection prepared by Tokuyasu method on a 600 μm wide optical waveguide. a Diffraction-limited chip-TIRFM image. In magenta, mitochondrial clusters immunolabeled with rabbit anti-Tomm20 protein (primary antibody) and Alexa Fluor 647-conjugated donkey anti-rabbit (secondary antibody). In green, actin segments labeled with Texas Red-X Phalloidin. In cyan, nuclei labeled with Sytox Green. **b** Scanning electron microscope image of the same region shown in (**a**) scanned at 30 nm pixel size. **c** high-magnification image of the white frame in (**a**) showing the diffraction-limited chip-TIRFM signal of mitochondria, actin, and nuclei. **d** CLEM image of areas in frames (**a**) and (**b**). Scanning electron microscope image acquired at 4 nm pixel size correlates with the MUSICAL images of mitochondria (magenta) and actin (green). **e** CLEM image of the white region in (**d**). MUSICAL image of the Tomm20 signal (magenta) in the outer membrane of mitochondria correlating with the morphology of the complex clusters of mitochondria. The tightly packed membranes of the outer segment are clearly recognized.
f CLEM image of MUSICAL-processed actin signal along with the outer segments (green) and three mitochondria clusters. The MUSICAL signal in (**d**–**f**) were gamma-corrected to increase the contrast of the actin ($\gamma = 1.2$) and the Tomm20 signal ($\gamma = 1.1$). Scale bars **a**, **b** 20 μm, **c**, **d** 5 μm, **e**, **f** 500 nm

vicinity to the chip are more susceptible to irreversible photodamage than those located further away, hence allowing for localized bleaching at the waveguide-sample interface. Remarkably, no labeling artifacts were observed when F-actin markers were used separately from their membrane counterparts (see Figs. 4, 5).

Next, the decaying nature of the evanescent field showed troublesome for chip-based SMLM acquisition. We found that upon increasing the laser power necessary for SMLM, not only stochastic emission occurred (as desired), but also a spontaneous fluorescent emission remained present through the image acquisition, decreasing the signal-to-background and thus hindering the localization precision of the dSTORM algorithm. We argue that, while the laser intensity at the waveguide-sample interface was strong enough to induce the photo-switching of the selected marker (namely, the CMDR), the intensity at the tail of the evanescent field reaching deeper into the sample was too weak to enable photo-switching, yet sufficient enough to support spontaneous fluorescence emission. Also, due to the construct of our optical system, we observed a low photon count of the blinking molecules which further compromised the SMLM reconstruction. We foresee that further efforts could minimize the undesired background signal by (a) avoiding unspecific fluorophore binding via waveguide surface functionalization; (b) employing advanced labeling techniques such as on-chip point accumulation imaging in nanoscale topography (DNA-PAINT)[34] to ensure low background signal; (c) employing thinner tissue samples (~100 nm) to fully exploit the maximum intensities of the evanescent field; (d) modifying the optical setup to improve the photon collection at the camera sensor. When it comes to improving the optical setup, replacing the current beam splitters with dichroic mirrors would allow a higher transmission rate for the emission spectrum of the fluorescent markers (see Supplementary Information S13).

We also encountered initial challenges obtaining consistent labeling repeatability. In particular, we observed significant variability in the staining quality throughout this study, even after following identical labeling protocols across various experiments. We found that the sucrose-methylcellulose droplet (used for the collection of the slices after cryosectioning) was masking the binding sites on the samples, thus reducing the antigenicity of the targeted proteins. We solved this issue by adjusting the initial washing steps of the cryoprotectant until successful staining was obtained. To this, different temperatures and incubation times were explored, according to existing preparation guidelines for Tokuyasu cryosections[57,61–63]. Hence, the samples for chip-based TIRFM, IFON, and SMLM were optimally labeled following incubation in phosphate-buffered saline (PBS) at 37 °C for 30 min, while the samples for chip-based CLEM were successfully stained after incubation in PBS at 0 °C for 20 min (see Supplementary Information S2).

Lastly, sectioning artifacts in the form of knife marks, tissue folds, and tissue rupture were also observed along with this study (see Supplementary Information S5). These problems were resolved by ensuring optimum blade sharpness on the cryo-ultramicrotome and by adjusting both the sectioning temperature and the slice thickness for each tissue type.

Discussion

In this study, we demonstrated the capabilities of the photonic chip as a feasible imaging platform for the morphological assessment of thin Tokuyasu sections of a variety of tissues. The photonic chip-based microscopy technique offers several advantages for histology: (a) it allows a broad range of imaging modalities over large fields of view including TIRFM, SMLM, IFON, and CLEM using a single standard optical microscope setup; (b) the imaging process can be seamlessly performed on conventional optical microscopes upon some modifications; (c) the photonic chip withstands all the chemical incubations and thermal conditions associated with the sample preparation. These features make the photonic chip an attractive platform for fluorescence-based histological investigations where high-throughput, high-contrast, and high-resolution are essential for the study of diseases[21]. In particular, we anticipate that upon specific labeling and image processing efforts, the photonic chip could assist both in reducing the processing time and in improving the assessment quality of histopathological analyses requiring sub-diffraction resolution. Despite optical nanoscopy probably not replacing the EM in these cases, we foresee that, by enabling more affordable and flexible imaging capabilities in terms of multi-modality and high-throughout, chip-based microscopy could potentially widen the adoption of optical nanoscopy for the diagnosis of diseases. Additionally, in CLEM experiments, the photonic chip could be used for fast assessment of ultrastructural preservation in tissues.

The photonic chip approach also reduces the complexity of the optical nanoscopy setups by miniaturization of the excitation light path, simplifying the implementation of multimodal imaging and facilitating a larger adoption of super-resolution microscopy in clinics and hospitals. In addition, the photonic chip can be mass-produced through standard semiconductor lithography processes, benefitting from low-cost manufacturing scalability. We foresee that further developments in coupling automation and the integration of microfluidics systems could dramatically improve the performance of the photonic chip platform, enabling more efficient and repeatable labeling, as well as fast multiplexed imaging.

Moreover, the implementation of advanced labeling strategies such as DNA-PAINT[34] and Exchange-PAINT[64] can effectively reduce the background signal, improve resolution, and support multiplexed acquisition. Also, on-chip technology facilitates the integration of other on-chip optical functions such as Raman spectroscopy[65], waveguide trapping[66], microfluidics[67], phase microscopy[27], among others.

While the photonic chip illumination strategy allows excitation over large areas, e.g., several centimeters in the present case, the light collection area is presently limited by the collection objective lens. Thus, it can be envisioned that the integration of microlens arrays[68] for light collection will open avenues that would make on-chip technology capable of handling the high-throughput imaging needed for routine histopathology. Moreover, the photonic chip can be designed and manufactured into standard microscope glass slide dimensions, allowing for a fully automated sample preparation through commercially available immunoassay analyzers, or via novel microfluidic techniques for multiplex immunofluorescence staining of clinically-relevant biomarkers[69].

Despite the encouraging imaging results obtained in this study, we acknowledge that the Tokuyasu samples represent a minority among the available histological methods. Also, we are aware that the maximum section area possible with the Tokuyasu cryosections (500 µm × 500 µm) may be insufficient for large-scale histopathological evaluation. However, this is an inherent limitation imposed by the sample preparation technique rather than the photonic chip imaging surface. Future chip-based histology studies should address the compatibility of this microscopy platform with widely accessible samples including FFPE and cryostat-sliced sections. Further, as stated in the CLEM section, chip-based microscopy can be exploited for volumetric observations of tissue sections via 3D-stacking of serial section imaging[59,60].

Materials and methods
Photonic chip description and fabrication

The photonic chip is composed of three layers: (i) a bottom silicon (Si) substrate, (ii) an intermediate cladding of silicon dioxide (SiO_2), and (iii) a top waveguide layer of a high refractive index material made of either silicon nitride (Si_3N_4, $n = 2.0$) or tantalum pentoxide (Ta_2O_5, $n = 2.1$) (see Fig. 1a). The high refractive index contrast (HIC) between the waveguide materials and the adjacent imaging medium and sample ($n \approx 1.4$), allows the confinement and propagation of the excitation light via total internal reflection (TIR), enabling chip-based total internal reflection fluorescence microscopy (chip-TIRFM) (Fig. 1c). Diverse geometries have been previously studied for chip-TIRFM, including slab, rib, and strip waveguides[23].

Here, we chose uncladded strip waveguides with heights ranging from 150 to 250 nm and widths varying from 200 to 1000 µm (see Fig. 1b).

In this study, we used both Si_3N_4 and Ta_2O_5 chips for chip-TIRFM imaging of tissue sections. While both materials exhibit similar optical and biocompatibility properties, the selection between Si_3N_4 and Ta_2O_5 was made purely on the availability of either type of chips. These were fabricated in distinct places: (i) the Si_3N_4 waveguide chips were manufactured according to CMOS fabrication process at the Institute of Microelectronics Barcelona (IMB-CNM, Barcelona, Spain) as detailed elsewhere[23,24]; (ii) the Ta_2O_5 chips were manufactured at the Optoelectronics Research Center (ORC, University of Southampton, UK), following the process herewith detailed[70]. Waveguides of 250 nm thickness were fabricated by deposition of Ta_2O_5 film on a commercially available 4" Si substrate having a 2.5 µm thick SiO_2 lower cladding layer (Si-Mat Silicon Materials, Germany) using a magnetron sputtering system (Plasmalab System 400, Oxford Instruments). The base pressure of the Ta_2O_5 deposition chamber was kept below 1×10^{-6} Torr with $Ar:O_2$ flow rates of 20 sccm: 5 sccm and the substrate temperature was maintained at 200 °C throughout the deposition process. Photolithography was used to create a photoresist mask for further dry etching to fabricate strip waveguides. First, 1 µm thick positive resist (Shipley, S1813) was coated on top of a 250 nm Ta_2O_5 film and then prebaked (1×30 min) at 90 °C. Then, the wafer was placed into a mask aligner (MA6, Süss MicroTec), and illuminated with the waveguide pattern. The Ta_2O_5 layer, which was not covered with photoresist, was fully etched to obtain strip waveguides of 250 nm height using an ion beam system (Ionfab 300+, Oxford Instruments) fed with argon at a flow rate of 6 sccm. The process pressure (2.3×10^{-4} Torr), beam voltage (500 V), beam current (100 mA), radiofrequency power (500 W), and substrate temperature (15 °C) were kept constant. Finally, the wafers were placed in a three-zone semiconductor furnace at 600 °C in an oxygen environment for 3 h (in batch) to reduce the stress and supplement the oxygen deficiency created in Ta_2O_5 during the sputtering and the etching process[31].

Upon reception, the wafers were split into individual chips using a cleaving system (Latticegear, LatticeAx 225). The remaining photoresist layer from the manufacturing process was removed by immersion in acetone (1×1 min). The chips were then cleaned in 1% Hellmanex in deionized water on a 70 °C hotplate (1×10 min), followed by rinsing steps with isopropanol and deionized water. The chips were finally dried with nitrogen using an air blowgun. To improve the adhesion of the tissue sections, the chips were rinsed with 0.1% w v^{-1} poly-L-lysine solution in H_2O and let dry in a vertical position (1×30 min).

Sample collection and preparation
Ethical statement

Both animal and human samples were handled according to relevant ethical guidelines. Healthy placental tissues were collected after delivery at the University Hospital of North Norway. Written consent was obtained from the participants following the protocol approved by the Regional Committee for Medical and Health Research Ethics of North Norway (REK Nord reference no. 2010/2058-4). Human kidney samples were anonymously obtained with written consent from the patients according to the protocol approved by the Regional Committee for Medical and Health Research Ethics of North Norway (REK Nord reference no. 2014/1693-1). Treatment and care of mice and pigs were conducted following the guidelines of the Norwegian Ethical and Welfare Board for Animal Research. Zebrafish experiments were conducted according to Swiss Laws and approved by the veterinary administration of the Canton of Zurich, Switzerland.

Preparation of Tokuyasu sections for chip-based TIRFM, IFON, and SMLM

Human placental and murine (NZBxNZW)F1 kidney tissue samples were cryopreserved following the Tokuyasu method for ultracryotomy described elsewhere[53,71]. In short, biopsies blocks of ~1 mm³ were collected, rinsed in 9 mg mL^{-1} sodium chloride, fixed in 8% formaldehyde at 4 °C overnight, infiltrated with 2.3 M sucrose at 4 °C overnight, mounted onto specimen pins, and frozen in liquid nitrogen. Thereafter, the samples were transferred to a cryo-ultramicrotome (EMUC6, Leica Microsystems) and sectioned with a diamond knife into thin slices ranging from 100 nm to 1 μm thickness. The sections were collected with a wire loop containing a 1:1 cryoprotectant mixture of 2% methylcellulose and 2.3 M sucrose and transferred to photonic chips coated with poly-ʟ-lysine and equipped with custom-made polydimethylsiloxane (PDMS) chambers of approximately 130 μm-height[24] (Fig. 1b). The samples were stored on Petri dishes at 4 °C before subsequent steps.

Diverse staining strategies were employed according to each imaging modality:

i. For Chip-based multicolor TIRFM imaging, human placental sections of 400 nm were direct-labeled for membranes, F-actin, and nuclei as described herewith. First, the cryoprotectant mixture was dissolved by incubating the samples in phosphate-buffered saline (PBS) (3 × 10 min) at 37 °C. Thereafter, the samples were incubated in a 1:2000 solution of CellMask Deep Red in PBS (1 × 15 min) at room temperature (RT) and subsequently washed with PBS (2 × 5 min). Next, the sections were incubated in 1:100 Phalloidin-Atto565 in PBS (1 × 15 min) and washed with PBS (2 × 5 min). Further, the samples were incubated in 1:500 Sytox Green in PBS (1 × 10 min) and washed with PBS (2 × 5 min). Finally, the sections were mounted with #1.5 coverslips using Prolong Diamond and sealed with Picodent Twinsil.

ii. For Chip-based SMLM imaging, mouse kidney cryosections of 400 nm were labeled for membranes and nuclei using CellMask Deep Red and Sytox Green, respectively, following identical concentrations and incubation steps as for the Chip-based multicolor TIRFM imaging experiments. To enable photoswitching of the fluorescent molecules, the samples were mounted with a water-based enzymatic oxygen scavenging system buffer as described in previous works[23,26]. Thereafter, the sections were covered with #1.5 coverslips and sealed with Picodent Twinsil.

iii. For Chip-based IFON imaging, human placental sections of 400 nm were prepared identically to the Chip-based multicolor TIRFM imaging experiment, except for the membrane labeling and subsequent washing steps that were omitted. In all cases, the labeled cryosections were stored at 4 °C and protected from light before imaging. Supplementary Information S6 provides a detailed description of the materials and reagents used in this protocol.

Preparation of Tokuyasu sections for chip-based CLEM

For Chip-based CLEM imaging, zebrafish eyes were prepared as described elsewhere[56]. Briefly, 5 days post-fertilization larvae were euthanized in tricaine and fixed with 4% formaldehyde and 0.025% glutaraldehyde in 0.1 M sodium cacodylate buffer (1 × 16 h) at 4 °C. Subsequently, eyes were dissected and washed in PBS, placed in 12% gelatin (1 × 10 min) at 40 °C, and finally left to harden at 4 °C. Embedded eyes were immersed in 2.3 M sucrose and stored at 4 °C before further storage in liquid nitrogen. Ultrathin sections of 110 nm thickness were obtained with a cryo-ultramicrotome (Ultracut EM FC6, Leica Microsystems) using a cryo-immuno diamond knife (35° - size 2 mm, Diatome). The cryosections were transferred to photonic chips fitted with a PDMS frame and stored at 4 °C before staining. The samples were incubated in PBS (1 × 20 min) at 0 °C, followed by two washing steps in PBS (2 × 2 min) at RT to dissolve the cryoprotectant. Then, the samples were preincubated with a blocking solution (PBG) for 5 min, followed by incubation (1 × 45 min) in a 1:50 solution of rabbit anti-Tomm20 in PBG blocking buffer at RT. After several rinsing (6 × 2 sec) and washing (1 × 5 min) in PBG, the specimens were incubated (1 × 45 min) with an Alexa Fluor 647-conjugated secondary donkey anti-rabbit antibody at 1:200 concentration in PBG at RT. For the acting staining, the samples were

washed in PBS (6 × 1 min), followed by incubation with Texas Red-X Phalloidin (1 × 10 min) at 1:50 concentration in PBS. After washes in PBS (2 × 5 min), the samples were incubated in a 1:500 solution of Sytox Green nuclear staining in PBS (1 × 10 min), followed by washes in PBS (2 × 5 min), and mounting with a 1:1 mixture of PBS and glycerol (49782, Sigma-Aldrich) and covered with a #1.5 glass coverslip before chip-TIRFM imaging. Supplementary Information S6 provides a detailed description of the materials and reagents used in this protocol.

Chip imaging and processing
Chip-based imaging

The chip-TIRFM setup was assembled using a modular upright microscope (BXFM, Olympus), together with a custom-built photonic chip module as shown in Fig. 1c and Supplementary Information S13. A fiber-coupled multi-wavelength laser light source (iChrome CLE, Toptica) was expanded and collimated through an optical fiber collimator (F280APC-A, Thorlabs) to fill the back aperture of the coupling MO (NPlan 50X/NA0.5, Olympus). Typical illumination wavelengths used were $\lambda_1 = 640$ nm, $\lambda_2 = 561$ nm, and $\lambda_3 = 488$ nm. Both the optical fiber collimator and the coupling objective were mounted on an XYZ translation stage (Nanomax300, Thorlabs) fitted with an XY piezo-controllable platform (Q-522 Q-motion, PI) for fine adjustments of the coupling light into the waveguides. The photonic chips were placed on a custom-made vacuum chuck fitted on an X-axis translation stage (XRN25P, Thorlabs) for large-range scanning of parallel waveguides. Fluorescent emission of the samples was achieved via evanescent field excitation upon coupling of the laser onto a chosen waveguide, as detailed elsewhere[23] (Fig. 1a, c). Various MO lenses were used to collect the fluorescent signal, depending on the desired FOV, magnification, and resolution (4X/0.1NA, 20X/0.45NA, and 60X/1.2NA water immersion). An emission filter set composed of a long-pass filter and a band-pass filter was used to block out the excitation signal at each wavelength channel (see Supplementary Information S13 for details). The emission signal passed through the microscope's 1X tube lens (U-TV1X-2, Olympus) before reaching the sCMOS camera image plane (Orca-flash4.0, Hamamatsu). Both the camera exposure time and the laser intensity were adjusted according to the experimental goal. For TIRFM imaging, the camera exposure time was set between 50 and 100 ms, and the input power was incrementally adjusted until the mean histogram values surpassed 500 counts. For SMLM, the acquisition time was set to 30 ms while the input power was set to its maximum level to enable photo-switching. Depending on the coupling efficiency, typical input powers were between 10 and 60% for TIRFM imaging, and between 90 to 100% for SMLM

imaging. To reduce photobleaching of the fluorescent markers, the image acquisition was sequentially performed from less energetic to more energetic excitation wavelengths. To deal with the anisotropic mode distribution of the multi-mode interference pattern at the waveguide, the coupling objective was laterally scanned at <1 μm steps over a 50–200 μm travel span along the input facet of the chip while individual images were taken. Image stacks of various sizes were acquired according to the imaging technique. Typically, 100–1000 frames for TIRFM and 30,000–50,000 frames for SMLM. White light from a halogen lamp (KL1600 LED, Olympus) was used for bright-field illumination to identify the regions of interest (ROI) through the collection objective. To reduce mechanical instability, the collection path of the system was fixed to the optical table, while the photonic chip module was placed onto a motorized stage (8MTF, Standa) for scanning across the XY directions. An optical table (CleanTop, TMC) was used as the main platform for the chip-TIRFM setup. Supplementary Information S13 offers a detailed description of the chip-TIRFM setup.

CLEM imaging

After chip-TIRFM imaging, both the coverslip and the PDMS frame were removed and the samples were fixed with 0.1% glutaraldehyde. Thereafter, the samples were incubated with methylcellulose followed by centrifugation at 4700 rpm (Heraeus Megafuge 40 R, Thermo Scientific) in a falcon tube. After drying (2 × 10 min) at 40 °C on a heating plate, the photonic chips were transferred to an electron beam evaporator (MED 020, Leica Microsystems). The specimen was then coated with platinum/carbon (Pt/C, 10 nm) by rotary shadowing at an angle of 8°[57]. Thereafter, the photonic chips were mounted on a 25 mm Pin Mount SEMclip (#16144-9-30, Ted Pella) and imaged at 4 nm pixel size with a scanning electron microscope (Auriga 40 CrossBeam, Carl Zeiss Microscopy) at a low-accelerating voltage (1.5 keV). Supplementary Information S14 illustrates various steps of SEM imaging on a photonic chip.

Image processing

The acquired frames were computationally processed on the open-source software Fiji[72] according to the desired imaging technique. To obtain diffraction-limited TIRFM images, the image stacks were computationally averaged using the Z Project tool. Thereafter, the averaged images were deconvolved with the DeconvolutionLab2 plugin[73], using a synthetic 2D point spread function (PSF) matching the effective pixel size of the optical system. Lastly, the Merge Channels tool was used to merge and pseudocolor independent averaged channels into a multicolor composite TIRFM image.

SMLM images were reconstructed using the thunder-STORM plugin[74]. For CLEM, the acquired TIRFM stacks were first processed with the NanoJ SRRF plugin[75] and then correlated with the EM images using the TrakEM2 plugin[76].

Author details
¹Department of Physics and Technology, UiT The Arctic University of Norway, Klokkargårdsbakken N-9019, Tromsø, Norway. ²Department of Clinical Medicine, Women's Health and Perinatology Research Group, UiT The Arctic University of Norway, Tromsø, Norway. ³Department of Obstetrics and Gynecology, University Hospital of North Norway, Tromsø, Norway. ⁴Center for Microscopy and Image Analysis, University of Zurich, Zürich, Switzerland. ⁵Division of Cardiothoracic and Respiratory Medicine, University Hospital of North Norway, Tromsø, Norway. ⁶Department of Clinical Medicine, Clinical Cardiovascular Research Group, UiT The Arctic University of Norway, Tromsø, Norway. ⁷Department of Medical Biology, RNA and Molecular Pathology Research Group, UiT The Arctic University of Norway, Tromsø, Norway. ⁸Division of Obstetrics and Gynecology, Department of Clinical Science, Intervention and Technology, Karolinska Institute, Stockholm, Sweden

Author contributions
BSA conceived the idea and supervised the project. LEVH. and VD planned and coordinated the experiments, performed sample labeling, chip-TIRFM imaging, and post-processing of the data. JCT, AA, and VD built the chip-based microscope setup. SA and KA performed MUSICAL reconstruction. DAC, VD, and LEVH. performed SMLM acquisition. DAC performed the dSTORM reconstruction. LEVH, JCT, and JMM performed chip-TIRFM imaging of the zebrafish eye. GB provided the zebrafish cryosections. GB, JMM, and UZ designed the experimental conditions for SEM imaging. JMM performed the SEM imaging for CLEM. FTD and AP respectively designed and fabricated the Ta₂O₅ photonic chips. GA provided the human placental sample. MN collected and preserved the human placental samples. GA and MN helped with the placental image interpretations. AMKH and KAF collected and preserved the mouse kidney tissue and assisted with the renal image interpretations. ÅBB collected and preserved the pig heart tissue and assisted with the cardiac image interpretation. LEVH. and VD analyzed the data, prepared the figures. LEVH, VD, and BSA wrote the manuscript. All authors contributed to writing and revising selected sections of the manuscript.

Conflict of interest
BSA has applied for a patent for chip-based optical nanoscopy and he is co-founder of the company Chip NanoImaging AS, which commercializes on-chip super-resolution microscopy systems.

References
1. Aeffner, F. et al. Digital microscopy, image analysis, and virtual slide repository. *ILAR J.* **59**, 66–79 (2018).
2. Redman, C. W. G. et al. Does size matter? Placental debris and the pathophysiology of pre-eclampsia. *Placenta* **33**, S48–S54 (2012).
3. Lange, K. Fundamental role of microvilli in the main functions of differentiated cells: outline of an universal regulating and signaling system at the cell periphery. *J. Cell. Physiol.* **226**, 896–927 (2011).
4. Unwin, P. N. T. & Zampighi, G. Structure of the junction between communicating cells. *Nature* **283**, 545–549 (1980).
5. Inaga, S. et al. Rapid three-dimensional analysis of renal biopsy sections by low vacuum scanning electron microscopy. *Arch. Histol. Cytol.* **73**, 113–125 (2011).
6. Micheva, K. D. & Smith, S. J. Array tomography: a new tool for imaging the molecular architecture and ultrastructure of neural circuits. *Neuron* **55**, 25–36 (2007).
7. Hell, S. W. et al. The 2015 super-resolution microscopy roadmap. *J. Phys. D Appl. Phys.* **48**, 443001 (2015).
8. Schermelleh, L., Heintzmann, R. & Leonhardt, H. A guide to super-resolution fluorescence microscopy. *J. Cell Biol.* **190**, 165–175 (2010).
9. Sahl, S. J., Hell, S. W. & Jakobs, S. Fluorescence nanoscopy in cell biology. *Nat. Rev. Mol. Cell Biol.* **18**, 685–701 (2017).
10. Heintzmann, R. & Huser, T. Super-resolution structured illumination microscopy. *Chem. Rev.* **117**, 13890–13908 (2017).
11. Willig, K. I. et al. STED microscopy reveals that synaptotagmin remains clustered after synaptic vesicle exocytosis. *Nature* **440**, 935–939 (2006).
12. Betzig, E. et al. Imaging intracellular fluorescent proteins at nanometer resolution. *Science* **313**, 1642–1645 (2006).
13. Rust, M. J., Bates, M. & Zhuang, X. W. Sub-diffraction-limit imaging by stochastic optical reconstruction microscopy (STORM). *Nat. Methods* **3**, 793–796 (2006).
14. Opstad, I. S. et al. Fluorescence fluctuations-based super-resolution microscopy techniques: an experimental comparative study. Preprint at *arXiv*:2008.09195v1 (2020).
15. Booth, M. et al. Aberrations and adaptive optics in super-resolution microscopy. *Microscopy* **64**, 251–261 (2015).
16. Baschong, W., Suetterlin, R. & Laeng, R. H. Control of autofluorescence of archival formaldehyde-fixed, paraffin-embedded tissue in confocal laser scanning microscopy (CLSM). *J. Histochem. Cytochem.* **49**, 1565–1571 (2001).
17. Creech, M. K., Wang, J., Nan, X. & Gibbs, S. L. Superresolution imaging of clinical formalin fixed paraffin embedded breast cancer with single molecule localization microscopy. *Sci. Rep.* **7**, 40766 (2017).
18. Wang, M. et al. High-resolution rapid diagnostic imaging of whole prostate biopsies using video-rate fluorescence structured illumination microscopy. *Cancer Res.* **75**, 4032–4041 (2015).
19. Ilgen, P. et al. STED super-resolution microscopy of clinical paraffin-embedded human rectal cancer tissue. *PLoS ONE* **9**, e101563 (2014).
20. Göttfert, F. et al. Coaligned dual-channel STED nanoscopy and molecular diffusion analysis at 20 nm resolution. *Biophys. J.* **105**, L01–L03 (2013).
21. Schlichenmeyer, T. C., Wang, M., Elfer, K. N. & Brown, J. Q. Video-rate structured illumination microscopy for high-throughput imaging of large tissue areas. *Biomed. Opt. Express* **5**, 366–377 (2014).
22. Agarwal, K. & Macháň, R. Multiple signal classification algorithm for super-resolution fluorescence microscopy. *Nat. Commun.* **7**, 13752 (2016).
23. Diekmann, R. et al. Chip-based wide field-of-view nanoscopy. *Nat. Photonics* **11**, 322–328 (2017).
24. Tinguely, J. C., Helle, Ø. I. & Ahluwalia, B. S. Silicon nitride waveguide platform for fluorescence microscopy of living cells. *Opt. Express* **25**, 27678–27690 (2017).
25. Opstad, I. S. et al. A waveguide imaging platform for live-cell TIRF imaging of neurons over large fields of view. *J. Biophotonics* **13**, e201960222 (2020).
26. Helle, Ø. I. et al. Nanoscopy on-a-chip: super-resolution imaging on the millimeter scale. *Opt. Express* **27**, 6700–6710 (2019).
27. Dubey, V. et al. Multi-modal chip-based fluorescence and quantitative phase microscopy for studying inflammation in macrophages. *Opt. Express* **26**, 19864–19876 (2018).
28. Coucheron, D. A. et al. High-throughput total internal reflection fluorescence and direct stochastic optical reconstruction microscopy using a photonic chip. *J. Vis. Exp.* https://doi.org/10.3791/60378-v (2019).

29. Agnarsson, B., Jonsdottir, A. B., Arnfinnsdottir, N. B. & Leosson, K. On-chip modulation of evanescent illumination and live-cell imaging with polymer waveguides. *Opt. Express* **19**, 22929–22935 (2011).

30. Griffiths, G., Slot, J. W. & Webster, P. Kiyoteru Tokuyasu: a pioneer of cryo-ultramicrotomy. *J. Microsc.* **260**, 235–237 (2015).

31. Priyadarshi, A. et al. A transparent waveguide chip for versatile total internal reflection fluorescence-based microscopy and nanoscopy. *Commun. Mater.* **2**, 85 (2021).

32. Mittler, S. In *Optics, Photonics and Laser Technology* (eds Ribeiro, P. A. & Raposo, M.) Ch. 1 (Springer, 2018).

33. Jayakumar, N., Helle, Ø. I., Agarwal, K. & Ahluwalia, B. S. On-chip TIRF nanoscopy by applying Haar wavelet kernel analysis on intensity fluctuations induced by chip illumination. *Opt. Express* **28**, 35454–35468 (2020).

34. Archetti, A. et al. Waveguide-PAINT offers an open platform for large field-of-view super-resolution imaging. *Nat. Commun.* **10**, 1267 (2019).

35. Helle, Ø. I. et al. Structured illumination microscopy using a photonic chip. *Nat. Photonics* **14**, 431–438 (2020).

36. Tinguely, J. C. et al. Photonic-chip assisted correlative light and electron microscopy. *Commun. Biol.* **3**, 739 (2020).

37. Silini, A. R. et al. Perinatal derivatives: where do we stand? A roadmap of the human placenta and consensus for tissue and cell nomenclature. *Front. Bioeng. Biotechnol.* **8**, 610544 (2020).

38. Tokuyasu, K. T. A technique for ultracryotomy of cell suspensions and tissues. *J. Cell Biol.* **57**, 551–565 (1973).

39. Tokuyasu, K. T. A study of positive staining of ultrathin frozen sections. *J. Ultrastruct. Res.* **63**, 287–307 (1978).

40. Loussert-Fonta, C. et al. Correlation of fluorescence microscopy, electron microscopy, and NanoSIMS stable isotope imaging on a single tissue section. *Commun. Biol.* **3**, 362 (2020).

41. Kopek, B. G. et al. Diverse protocols for correlative super-resolution fluorescence imaging and electron microscopy of chemically fixed samples. *Nat. Protoc.* **12**, 916–946 (2017).

42. Askelund, K. J. & Chamley, L. W. Trophoblast deportation part I: review of the evidence demonstrating trophoblast shedding and deportation during human pregnancy. *Placenta* **32**, 716–723 (2011).

43. King, B. F. The organization of actin filaments in human placental villi. *J. Ultrastruct. Res.* **85**, 320–328 (1983).

44. van de Linde, S. et al. Direct stochastic optical reconstruction microscopy with standard fluorescent probes. *Nat. Protoc.* **6**, 991–1009 (2011).

45. Carlson, E. C. et al. Significant glomerular basement membrane thickening in hyperglycemic and normoglycemic diabetic-prone BB Wistar rats. *Anat. Rec. A Discov. Mol. Cell. Evol. Biol.* **281**, 1308–1318 (2004).

46. Chi, W. et al. Descriptor ΔGC-O enables the quantitative design of spontaneously blinking rhodamines for live-cell super-resolution imaging. *Angew. Chem.* **132**, 20390–20398 (2020).

47. Uno, S. N. et al. A spontaneously blinking fluorophore based on intramolecular spirocyclization for live-cell super-resolution imaging. *Nat. Chem.* **6**, 681–689 (2014).

48. Darouich, S. et al. Value of electron microscopy in the diagnosis of glomerular diseases. *Ultrastruct. Pathol.* **34**, 49–61 (2010).

49. Shore, I. & Moss, J. Electron microscopy in diagnostic renal pathology. *Curr. Diagnostic Pathol.* **8**, 207–215 (2002).

50. Miura, S. et al. Fluid shear triggers microvilli formation via mechanosensitive activation of TRPV6. *Nat. Commun.* **6**, 8871 (2015).

51. Acuña, S. et al. Soft thresholding schemes for multiple signal classification algorithm. *Opt. Express* **28**, 34434–34449 (2020).

52. Descloux, A., Grußmayer, K. S. & Radenovic, A. Parameter-free image resolution estimation based on decorrelation analysis. *Nat. Methods* **16**, 918–924 (2019).

53. Villegas-Hernández, L. E. et al. Visualizing ultrastructural details of placental tissue with super-resolution structured illumination microscopy. *Placenta* **97**, 42–45 (2020).

54. Wang, M. et al. Gigapixel surface imaging of radical prostatectomy specimens for comprehensive detection of cancer-positive surgical margins using structured illumination microscopy. *Sci. Rep.* **6**, 27419 (2016).

55. Johnson, K. A. & Hagen, G. M. Artifact-free whole-slide imaging with structured illumination microscopy and Bayesian image reconstruction. *GigaScience* **9**, giaa035 (2020).

56. Mateos, J. M. et al. Correlative super-resolution and electron microscopy to resolve protein localization in zebrafish retina. *J. Vis. Exp.* https://doi.org/10.3791/56113 (2017).

57. Mateos, J. M. et al. Topographic contrast of ultrathin cryo-sections for correlative super-resolution light and electron microscopy. *Sci. Rep.* **6**, 34062 (2016).

58. Link, B. A. & Collery, R. F. Zebrafish models of retinal disease. *Annu. Rev. Vis. Sci.* **1**, 125–153 (2015).

59. Reichelt, M. et al. 3D reconstruction of VZV infected cell nuclei and PML nuclear cages by serial section array scanning electron microscopy and electron tomography. *PLoS Pathog.* **8**, e1002740 (2012).

60. Arganda-Carreras, I., Fernández-González, R., Muñoz-Barrutia, A. & Ortiz-De-Solorzano, C. 3D reconstruction of histological sections: application to mammary gland tissue. *Microsc. Res. Tech.* **73**, 1019–1029 (2010).

61. Slot, J. W. & Geuze, H. J. Cryosectioning and immunolabeling. *Nat. Protoc.* **2**, 2480–2491 (2007).

62. van Rijnsoever, C., Oorschot, V. & Klumperman, J. Correlative light-electron microscopy (CLEM) combining live-cell imaging and immunolabeling of ultrathin cryosections. *Nat. Methods* **5**, 973–980 (2008).

63. Griffith, J. M. & Posthuma, G. A reliable and convenient method to store ultrathin thawed cryosections prior to immunolabeling. *J. Histochem. Cytochem.* **50**, 57–62 (2002).

64. Werbin, J. L. et al. Multiplexed exchange-PAINT imaging reveals ligand-dependent EGFR and Met interactions in the plasma membrane. *Sci. Rep.* **7**, 12150 (2017).

65. Løvhaugen, P., Ahluwalia, B. S., Huser, T. R. & Hellesø, O. G. Serial Raman spectroscopy of particles trapped on a waveguide. *Opt. Express* **21**, 2964–2970 (2013).

66. Helle, Ø. I., Ahluwalia, B. S. & Hellesø, O. G. Optical transport, lifting and trapping of micro-particles by planar waveguides. *Opt. Express* **23**, 6601–6612 (2015).

67. Wang, X. et al. Enhanced cell sorting and manipulation with combined optical tweezer and microfluidic chip technologies. *Lab Chip* **11**, 3656–3662 (2011).

68. Orth, A. & Crozier, K. Gigapixel fluorescence microscopy with a water immersion microlens array. *Opt. Express* **21**, 2361–2368 (2013).

69. Cappi, G., Dupouy, D. G., Comino, M. A. & Ciftlik, A. T. Ultra-fast and automated immunohistofluorescent multistaining using a microfluidic tissue processor. *Sci. Rep.* **9**, 4489 (2019).

70. Ahluwalia, B. S. et al. Fabrication of submicrometer high refractive index tantalum pentoxide waveguides for optical propulsion of microparticles. *IEEE Photonics Technol. Lett.* **21**, 1408–1410 (2009).

71. Fenton, K. et al. Anti-dsDNA antibodies promote initiation, and acquired loss of renal Dnase1 promotes progression of lupus nephritis in autoimmune (NZBxNZW)F1 mice. *PLoS ONE* **4**, e8474 (2009).

72. Schindelin, J. et al. Fiji: an open-source platform for biological-image analysis. *Nat. Methods* **9**, 676–682 (2012).

73. Sage, D. et al. DeconvolutionLab2: an open-source software for deconvolution microscopy. *Methods* **115**, 28–41 (2017).

74. Ovesný, M. et al. ThunderSTORM: a comprehensive ImageJ plug-in for PALM and STORM data analysis and super-resolution imaging. *Bioinformatics* **30**, 2389–2390 (2014).

75. Gustafsson, N. et al. Fast live-cell conventional fluorophore nanoscopy with ImageJ through super-resolution radial fluctuations. *Nat. Commun.* **7**, 12471 (2016).

76. Cardona, A. et al. TrakEM2 software for neural circuit reconstruction. *PLoS ONE* **7**, e38011 (2012).